

Understanding Potential-dependent Competition Between Electrocatalytic Dinitrogen and Proton Reduction Reactions

Changhyeok Choi

Korea Advanced Institute of Science and Technology

Geun Ho Gu

Korea Advanced Institute of Science and Technology

Juhwan Noh

Korea Advanced Institute of Science and Technology

Hyun S. Park

Korea Institute of Science and Technology

Yousung Jung (✉ ysjn@kaist.ac.kr)

Korea Advanced Institute of Science and Technology <https://orcid.org/0000-0003-2615-8394>

Article

Keywords: electrocatalytic dinitrogen, proton reduction reactions, electrochemical N₂ reduction reaction (NRR), hydrogen evolution reaction (HER)

Posted Date: April 21st, 2021

DOI: <https://doi.org/10.21203/rs.3.rs-140083/v1>

License:  This work is licensed under a Creative Commons Attribution 4.0 International License.

[Read Full License](#)

Version of Record: A version of this preprint was published at Nature Communications on July 16th, 2021. See the published version at <https://doi.org/10.1038/s41467-021-24539-1>.

Understanding Potential-dependent Competition Between Electrocatalytic Dinitrogen and Proton Reduction Reactions

Changhyeok Choi^{1‡}, Geun Ho Gu^{1‡}, Juhwan Noh¹, Hyun S. Park², and Yousung Jung^{1*}

¹Department of Chemical and Biomolecular Engineering Korea Advanced Institute of Science and Technology (KAIST) 291 Daehak-ro, Yuseong-gu, Daejeon 34141, Republic of Korea

²Center for Hydrogen and Fuel Cell Research, Korea Institute of Science and Technology (KIST), Seoul 02792, Republic of Korea

*To whom correspondence may be addressed via e-mail: ysjn@kaist.ac.kr

‡These authors contributed equally to this work

Abstract

One of the key challenges to practical electrochemical N₂ reduction reaction (NRR) is to lower the overpotential and suppression of the side reaction known as the hydrogen evolution reaction (HER) during the NRR. The experimental NRR activity has been consistently shown to reach a maximum at early stage before reaching the mass-transfer limit and decreases with large overpotentials for many heterogeneous catalysts. Though the volcano-type current-potential relationship shown for NRR is unusual with limited reaction rates at higher overpotentials, the mechanistic origin has not been clearly explained, making the design principles for practical NRR still lacking. Herein, we investigate the potential-dependent reaction activity of NRR and HER using the constant electrode potential method and microkinetic modeling. It manifests the dominating proton adsorption over dinitrogen at

small overpotentials leading to the inadequate reaction selectivity towards NRR at many metal catalyst surfaces. A clear potential-dependent competition between the N₂ adsorption and *H formation is characterized by the degree of charge transfer in the adsorption process. It is also demonstrated that the larger charge transfer in *H formation is *a general phenomenon* applied to all heterogeneous catalyst surfaces considered here, that poses a fundamental challenge to realize practical electrochemical NRR. We suggest several strategies to overcome the latter challenges based on the present understandings.

Introduction

Ammonia, the main source of nitrogen fertilizers, is one of the most produced chemicals in the world (e.g. 150 million metric tons in 2019)¹. Ammonia has been primarily produced by the Haber-Bosch process, proceeding via the net reaction of $\text{N}_2 + 3\text{H}_2 \rightarrow 2\text{NH}_3$. In order to dissociate the strong N≡N triple bond of N₂, and shift the equilibrium towards ammonia, the Haber-Bosch process typically requires harsh conditions of ~400 °C and ~150 bar². Hence, ammonia production is responsible for 1~2 % of worldwide energy consumption. Also, a large amount of fossil fuel is consumed to produce H₂ and it accounts for over 1 % of global energy-related CO₂ emissions^{3,4}. To solve the energy and environment-related problems in ammonia production, the method that operates at low temperatures and milder conditions is highly needed.

Electrochemical N₂ reduction reaction (NRR) produces ammonia cleanly and sustainably via the net reaction of $\text{N}_2 + (6\text{H}^+ + \text{e}^-) \rightarrow 2\text{NH}_3$ at ambient conditions. Various catalysts have demonstrated NRR activity at room temperatures, but the yield rate and the faradaic

efficiency (<10%) are too low for the economic production, due mainly to unwanted side reactions, hydrogen evolution reaction (HER)⁵. Theoretical studies have suggested that the theoretical limiting potential (U_L) where the electrochemical reaction becomes exothermic, for NRR is about -1 V for various catalysts and is much more negative than U_L of HER⁶. Thus, HER is expected to proceed before NRR when lowering the potential.

More quantitatively, however, potential-dependent measurements often showed that the NRR activity (NH_3 yield rate) begins to decrease even at a low overpotential region⁷. For numerous catalysts (Supplementary Note 1 and Supplementary Table S1), including transition metal⁸⁻¹¹, single-atom catalyst (SAC)¹²⁻¹⁷, transition metal oxides^{18,19} and non-metal catalysts²⁰⁻²², the maximum NRR activity (both faradaic efficiency and yield rate) has been generally observed with insignificant overpotentials, i.e. approximately 200 mV, then decreased at large overpotentials before reaching the mass-transfer limit. It results in the NRR current much smaller than the expected mass-transfer limited values considering saturated N_2 concentration in aqueous solution at ambient conditions, i.e. approximately 1 mM⁷.

The potential-dependent NRR activity is also different from other electrochemical reactions such as an electrochemical CO_2 reduction reaction (CO_2RR). CO_2RR also competes with HER during the reaction. We compare the catalytic activity for NRR and CO_2RR at Fe single-atomic site embedded at N-doped graphene (denoted as Fe@N₄), which was reported as an active catalyst for both NRR and CO_2RR ^{13,23,24}. Here, we estimate CO_2RR activity and NRR activity by using turnover frequency (TOF) of CO formation and NH_3 yield rate, respectively. From our density functional theory (DFT) calculations, U_L for CO_2RR and NRR is -0.32 V and -1.29 V, respectively (Fig. 1a). Thus, NRR is predicted to be facilitated at more negative potential than CO_2RR . Contrary to this prediction, the maximum CO_2RR activity was obtained at more

negative U than NRR (Fig. 1b). The maximum CO₂RR activity is observed at around -0.7 V ²⁴, more negative than U_L (-0.32 V). At $U = -0.7\text{ V}$ which is more negative than U_L , CO₂RR can be sufficiently facilitated. However, NRR activities begin to decrease at -0.4 V (pH = 7.2) or -0.05 V (pH = 13), before reaching its U_L (-1.29 V). This result indicates that NRR activity prematurely decreases with increasing reduction potential while its kinetics has not reached its expected theoretically maximum. Thus the premature decrease in the NRR activity should be attributed to the intrinsic properties of catalysts.

The premature decrease of NRR activity indeed hampers to obtain reasonable NH₃ yield rate at the potential region where the NRR is expected to be sufficiently facilitated, and should be the reason for the significantly lower NH₃ yield rates in all reported cases compared to other electrochemical reactions such as CO₂RR. In the case of Fe@N₄, for example, the reported yield rate of CO formation and NH₃ formation is $\sim 21\text{ mmol h}^{-1}\text{ m}^{-2}$ ²⁴ and $0.562\text{ mmol h}^{-1}\text{ m}^{-2}$ ¹³, respectively. To understand such an unusual behavior of NRR, a fundamental understanding of potential-dependent changes in reaction energetics and coverage is required.

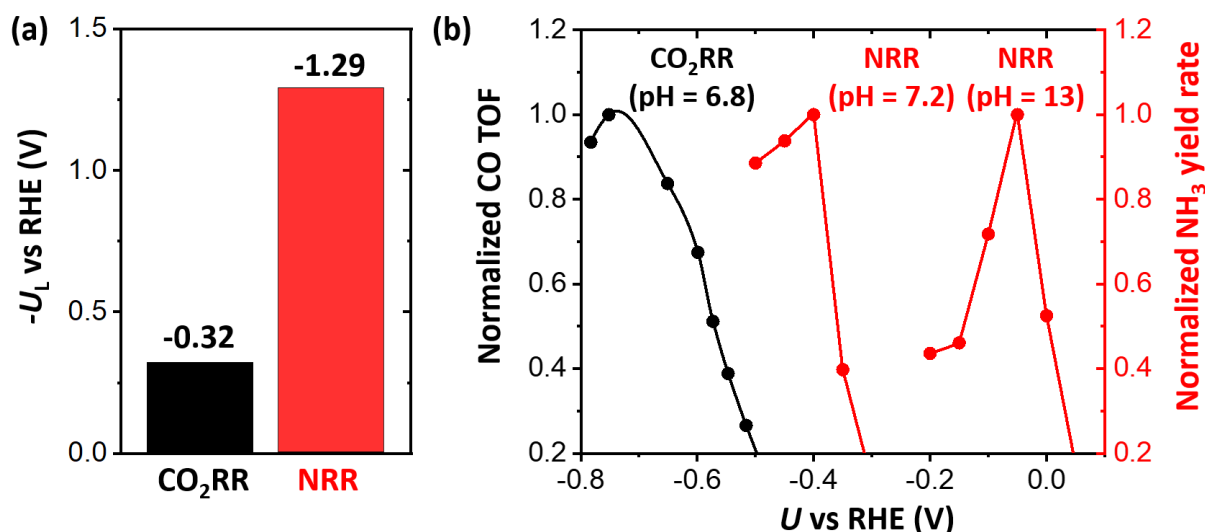


Fig. 1 / Comparison of onset potential for CO_2RR and that for NRR on Fe@N_4 catalysts. (a) U_L for CO_2RR (black, CO formation) and NRR (red, NH_3 formation) obtained on the Fe single atom embedded N-doped graphene using DFT calculations with the CHE model. (b) Potential-dependent measurements of turnover frequency (TOF) of CO in CO_2RR (black) and NH_3 yield rate in NRR (red) taken from the literature; CO TOF (pH = 6.8) is taken from Ju et al.²⁴ and NH_3 yield rates at pH = 7.2 and pH = 13 are taken from Lü et al.²³ and Zhang et al.¹³. Normalized CO TOF and NH_3 yield rates are obtained by dividing their absolute values with its maximum.

Here, we attempt to quantify the effect of potential-dependent surface coverage on the NRR activity and unveil the origin of premature decrease of NRR activity. We note that while many theoretical studies investigated the details of NRR mechanisms on catalysts such as $\text{Ru}^{25,26}$, Fe^{27} , transition metal nitrides²⁸⁻³⁰ and late transition metal surfaces³¹, these studies did not investigate the potential-dependent behavior of NRR discussed above, and used neutral state density functional theory (DFT) calculations with the computational hydrogen electrode (CHE) model³². In the CHE model, due to the constant charge constraint, the workfunction (or chemical potential) of the system changes from reactants to transition states (or final states) and fractional charge transfer is not allowed. This makes the CHE model, albeit widely used and proven successful for designing new catalysts and enhancing our understanding, not

suitable for interpreting the experimentally observed potential-dependent behaviors of electrochemical catalysis.

In this work, we use the constant electrode potential (CEP) model³³⁻³⁹ in conjunction with DFT to investigate the competitive kinetics of NRR and HER. In the CEP model, the number of electrons is adjusted to guarantee different states to have the same workfunction in the grand canonical states. We compute energetics of NRR and HER as a function of electrode potential (U) for a single Fe atom catalyst embedded in N-doped graphene (Fe@N₄) as a model system (but the generalized discussion for other catalysts are given later in the paper). The calculated potential-dependent reaction energetics are then used in the microkinetic modeling (MKM) to obtain the active site coverages and yield rate measurements to compare them with experiments. Remarkably, we find a potential-dependent crossover between the H binding and N₂ binding energies, leading to a crossover in the active site coverages and NH₃ yield rate behaviors, all consistent with experiments. Further analysis demonstrates that the latter crossover originates from the larger charge transfer in the *H formation than that of *N₂ and *NNH formation. Further calculations on other catalysts reveal that the larger charge transfer in *H compared to *N₂ and *NNH formation is indeed a general trend. We then discuss several directions to overcome this fundamental challenge of activity drop for NRR as a function of potential.

Results

Calculation models. We choose Fe single atomic site anchored by four N atoms in the graphene (denoted as Fe@N₄) as a model system since there are several well-characterized

(including the isotope $^{15}\text{N}_2$ measurements) experimental results to compare^{13,14,23}. As described above, Fe@N₄ catalysts showed volcano-shaped NRR activity with respect to the U . In the NRR measurements on Fe@N₄, the maximum NH₃ yield rate is obtained at $U = 0, -0.05$ V (vs. RHE) in 0.1 M KOH^{13,14} and $U = -0.40$ V (vs. RHE) in 0.1 M phosphate-buffered saline (PBS)²³. To calculate the potential-dependent activation energy in electrochemical reactions, we include a hexagonal ice bilayer (H-down geometry)⁴⁰⁻⁴² above the Fe@N₄ site (Fig. 2). Here, three different reaction conditions (acidic, neutral and alkaline) were considered. We use H₂O as a proton donor in neutral and alkaline conditions, while we use solvated hydronium ion (H₃O⁺) as a proton donor in acidic condition.

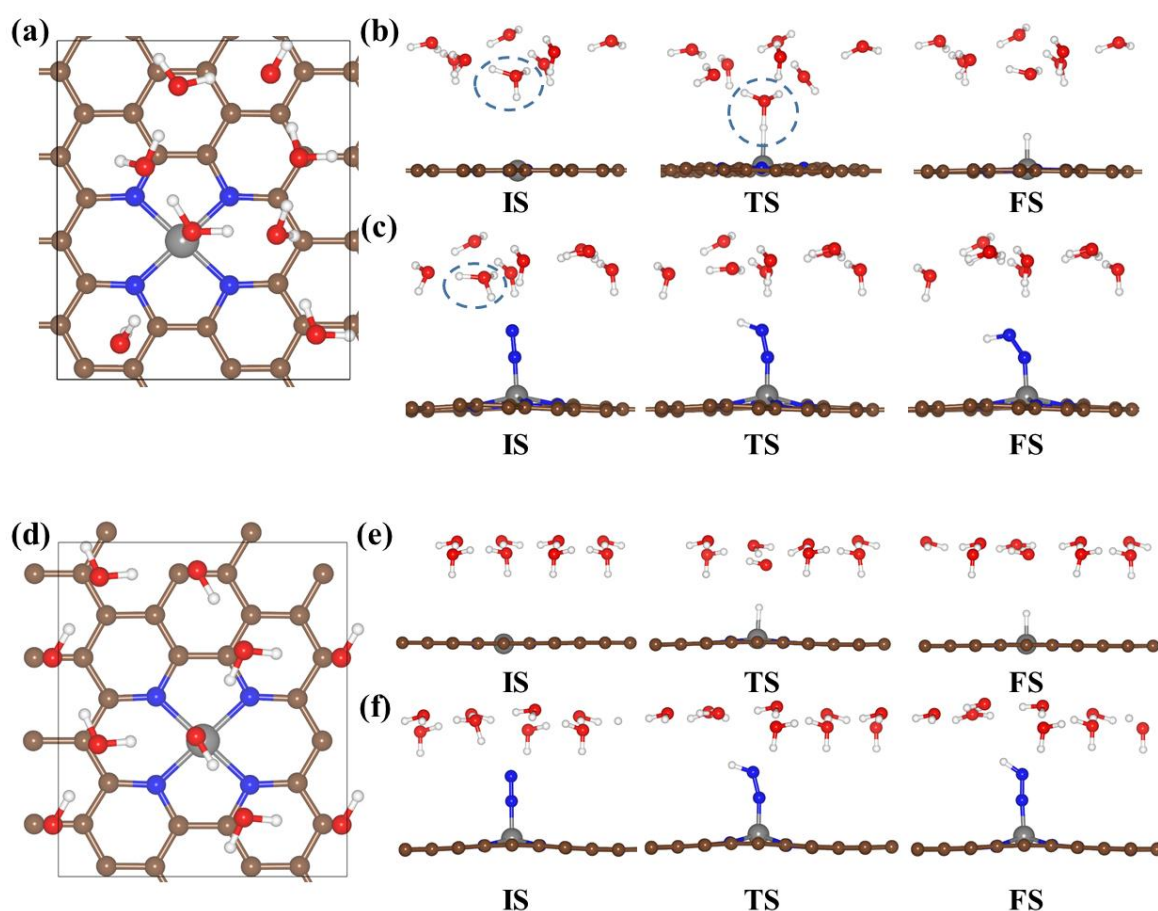


Fig. 2 | Calculation models for Fe@N₄ catalysts. Top-view of (a) Fe@N₄ with a hexagonal ice bilayer water containing a solvated H₃O⁺, initial state (IS), transition state (TS) and final state (FS) for (b) *H formation and (c) *NNH formation, respectively in acidic condition. The

solvated H_3O^+ in acidic condition is represented in dashed circle. Top-view of (d) Fe@N_4 with a hexagonal ice bilayer water, initial state (IS), transition state (TS) and final state (FS) for (e) $^*\text{H}$ formation and (f) $^*\text{NNH}$ formation, respectively in neutral or alkaline condition. Grey, blue, brown, red and white balls represent Fe, N, C, O and H atoms, respectively.

Potential-dependent energetics. We first compare the free energy change for $^*\text{N}_2$ and $^*\text{H}$ formation (* denoting the adsorbed species) on Fe@N_4 at different electrode potentials (U) (Fig. 3), the first reaction step for NRR and HER, respectively. $\Delta G_a^\ddagger(^*\text{H})$, $\Delta G(^*\text{H})$, and $\Delta G(^*\text{N}_2)$ represent activation free energy for $^*\text{H}$ formation, reaction free energy for $^*\text{H}$ formation and N_2 adsorption, respectively. Calculation details for obtaining ΔG_a^\ddagger are shown in Supplementary Note 2.

At 0 V, which is close to the equilibrium potential of NRR at standard state (0.057 V vs. RHE), $\Delta G(^*\text{N}_2)$ is more negative than $\Delta G(^*\text{H})$ (Fig. 3a). With more negative potential, $\Delta G(^*\text{N}_2)$, $\Delta G_a^\ddagger(^*\text{H})$ and $\Delta G(^*\text{H})$ all become more negative (favorable for reaction), but the $\Delta G_a^\ddagger(^*\text{H})$ and $\Delta G(^*\text{H})$ changes faster than $\Delta G(^*\text{N}_2)$. The slope (ΔG vs. U) increases in the order of $\Delta G(^*\text{N}_2)$ (0.19) < $\Delta G_a^\ddagger(^*\text{H})$ (0.79 and 0.96) < $\Delta G(^*\text{H})$ (1.18). Due to this difference, a crossover in which $\Delta G(^*\text{N}_2) = \Delta G(^*\text{H})$ occurs at potential $U_{\text{cross}} = -0.15$ V. This result would indicate a strong dependency of N_2 coverage (θ_{N_2}) on U . At $U > U_{\text{cross}}$, θ_{N_2} will be higher than H coverage (θ_{H}), while at $U < U_{\text{cross}}$, H coverage could overwhelm θ_{N_2} and hinder the NRR. Actual coverages as a function of potential are calculated and discussed in further detail with microkinetic modeling in the next section.

Next, we analyze the trend of NRR and HER activity by comparing $\Delta G_a^\ddagger(^*\text{NNH})$ and $\Delta G_a^\ddagger(^*\text{H})$, a potential-determining step in NRR and HER on Fe@N_4 (Supplementary Note 3 and Supplementary Fig. 3-4), respectively. Here, $\Delta G_a^\ddagger(^*\text{NNH})$ (or $\Delta G(^*\text{NNH})$) represents activation

energy (or reaction energy) of $*N_2 + (H^+ + e^-) \rightarrow *NNH$. We find that $\Delta G_a^\ddagger(*NNH)$ (or $\Delta G(*NNH)$) decreases with negative U , indicating that the NRR activity would increase with more negative potential (Fig. 3b). However, ΔG_a^\ddagger as well as ΔG for $*NNH$ formation are higher than those of $*H$ formation. For both proton donors (H_3O^+ and H_2O), $\Delta G_a^\ddagger(*NNH)$ is higher than $\Delta G_a^\ddagger(*H)$ (Fig. 3b) and their differences get even larger with more negative potential (Supplementary Note 4 and Supplementary Fig. 8-9). This result indicates that the rate of NRR is lower than that of HER in both acidic and alkaline conditions, and the rate of HER with potential grows even faster than that of NRR rate with potential. Consequently, the hindering effect of HER would become increasingly more important with negative potential.

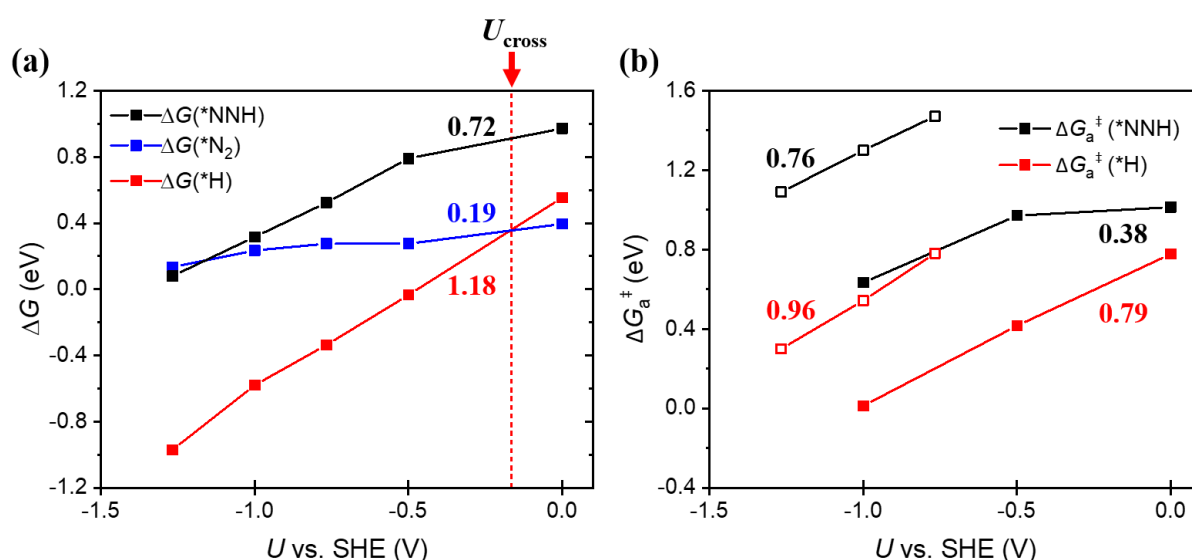


Fig. 3 | Potential-dependent change of activation energies and reaction energies for $*H$ formation, N_2 adsorption and $*NNH$ formation. (a) Change of $\Delta G(*NNH)$, $\Delta G(*N_2)$ and $\Delta G(*H)$ by U . The red horizontal dashed lines in (a) represents the crossover potential (U at $\Delta G(*H) = \Delta G(*N_2)$). (b) Change of $\Delta G_a^\ddagger(*NNH)$ and $\Delta G_a^\ddagger(*H)$ by U . The slope (ΔG vs. U or ΔG_a^\ddagger vs. U) of each reaction is shown in the graph. Opened and closed square represent ΔG_a^\ddagger obtained by using H_2O and H_3O^+ as a proton donor, respectively. Black, blue and red lines represent reaction energetics for $*NNH$, $*N_2$ and $*H$ formation, respectively.

Microkinetic modeling. To further investigate how the surface coverages and NRR activity change by U , we performed a microkinetic modeling (MKM) based on the potential-

dependent energetics of NRR and HER obtained from the CEP model (Fig. 4) described above. The details on the MKM are in Supplementary Note 5. Since the NRR activity was measured at pH = 13 (0.1 M KOH)^{13,14} and pH = 7.2 (0.1 M phosphate-buffered saline)²³ in the experiments (Fig. 1), we note that the MKM results under alkaline, neutral and acidic condition are represented in RHE scale at pH = 13, pH = 7.2 and pH = 0, respectively. Here, we use relative NH₃ yield rate rather than absolute one due to the inherent uncertainties in quantifying reaction rates from both experiment and theory⁴³. The relative NH₃ yield rate is obtained by normalizing the values by its maximum.

For all reaction conditions, we find that the relative NH₃ yield rate (denoted as r_{NH_3}) has a volcano-shape at the low overpotential region (Fig. 4), similar to the experiments (Fig. 1). The maximum r_{NH_3} is obtained at -0.25 V (pH = 0 and pH = 13) and -0.58 V (pH = 7.2). Interestingly, this U at maximum r_{NH_3} (-0.25 ~ -0.58 V) is highly more positive than theoretical limiting potential (U_L) for NRR of -1.29 V (Supplementary Fig. 3), indicating that the r_{NH_3} decreases prematurely even before reaching the theoretical limiting potential needed to drive the reaction. Noticeably, the θ_{N_2} also has a volcano shape and the U at maximum θ_{N_2} is very similar, differing by ~ 0.1 V from the U at maximum r_{NH_3} (Supplementary Table 4). This result indicates that the premature maximum in r_{NH_3} at substantially more positive potential originates from the decrease in θ_{N_2} . Contrary to θ_{N_2} , θ_{H} increases continuously and we find a crossover in coverages between θ_{N_2} and θ_{H} as predicted by the crossover between $\Delta G(^*\text{H})$ and $\Delta G(^*\text{N}_2)$ (Fig. 3). We emphasize that the premature decreases of r_{NH_3} and θ_{N_2} are consistently observed at alkaline, neutral and acidic conditions, indicating that such a phenomenon occurs pH-independently.

To further estimate the effect of HER on potential-dependent behavior of NRR, we performed the MKM simulations without considering HER, corresponding to an ideal environment in which NRR proceeds without competing with HER. The r_{NH_3} without HER is obtained by normalizing the values with the maximum value of r_{NH_3} with HER. Without the HER, the premature decrease of r_{NH_3} and θ_{N_2} are not observed (Fig. 4). We find that the r_{NH_3} and θ_{N_2} continuously increases with negative U in all reaction conditions, clearly suggesting that the occurrence of early maximum in r_{NH_3} originates from the decreasing θ_{N_2} by the competing HER. Furthermore, r_{NH_3} and θ_{N_2} obtained by MKM without HER are higher than those with HER at all potential ranges, confirming that the HER indeed hampers the NRR.

We are now in a position to understand the origin of premature decrease of r_{NH_3} and potential-dependent competition with HER. At lower overpotentials where the θ_{N_2} is more dominant than θ_{H} , increasing θ_{N_2} and decreasing $\Delta G_a^\ddagger(*\text{NNH})$ with negative U results in the increasing r_{NH_3} (Fig. 3 and Fig. 4). At higher overpotentials, although $\Delta G_a^\ddagger(*\text{NNH})$ continuously decreases, the θ_{H} becomes high enough to block active sites and reduces θ_{N_2} . Consequently, the electrode potential of maximum r_{NH_3} is close to the potential of maximum θ_{N_2} (Supplementary Table 4), and after reaching the maximum, the r_{NH_3} decreases due to decreasing θ_{N_2} with more negative potential. These results clearly demonstrate that potential-dependent θ_{N_2} is the underlying mechanism for the potential-dependent NH_3 yield rate behavior.

In the MKM simulations, the maximum r_{NH_3} is observed at $U = -0.25$ V (pH = 13) and -0.58 V (pH = 7.2), respectively. This is similar to the experimental value at pH = 13 (0.0 V and -0.05 V)^{13,14} and pH = 7.2 (-0.40 V)²³, qualitatively explaining the experimental trend. Due to the intrinsic DFT error especially significant in ionic species⁴⁴ and different environments from

experiments, such as explicit electrolytes and local pH, we note that such a difference is acceptable. However, a sharp increase and decrease of r_{NH_3} at low overpotential region is well reproduced in our MKM simulations. Interestingly, U at maximum r_{NH_3} obtained by the MKM is significantly more positive than the U_L for NRR (-1.29 V) (Supplementary Fig. 3). This suggests that considering the U_L only is insufficient to fully understand NRR behavior and explains why the reported theoretical U_L has been disagreed with experiments⁴⁵, but instead, the potential-dependent competition between NRR and HER should be considered.

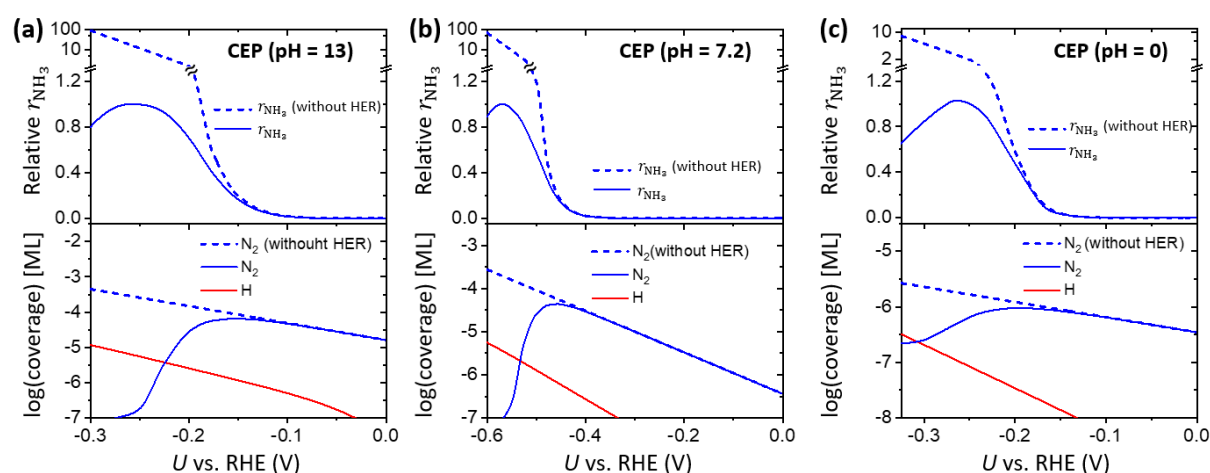


Fig. 4 | The change in θ_{N_2} , θ_{H} and r_{NH_3} by U obtained by the microkinetic modeling (MKM) using the CEP model. At (a) pH = 13, (b) pH = 7.2 and (c) pH = 0. The relative r_{NH_3} is obtained by dividing the r_{NH_3} by its maximum. Dashed lines represent MKM results without HER. The relative r_{NH_3} and coverage are shown in upper and lower panels, respectively.

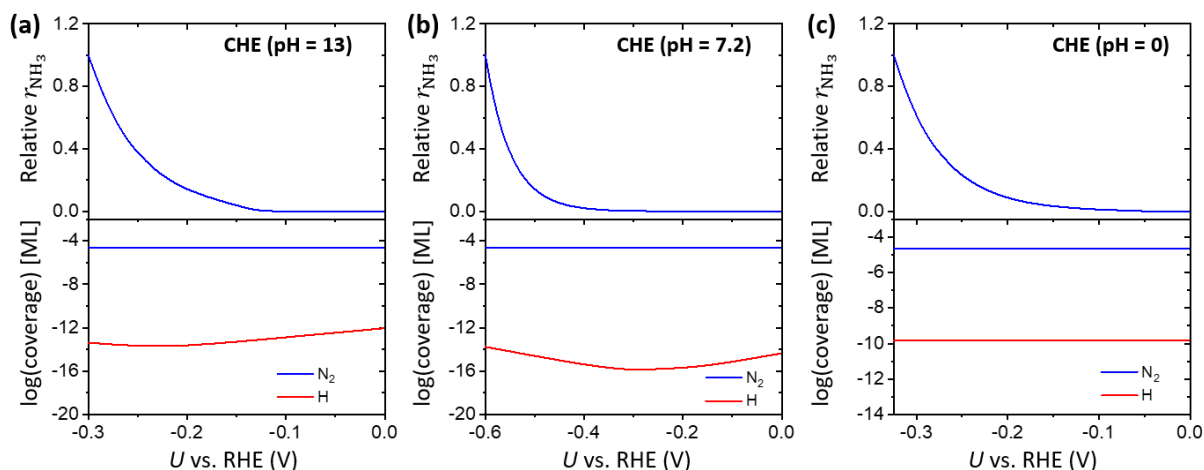


Fig. 5 | The change in θ_{N_2} , θ_H and r_{NH_3} by U obtained by the microkinetic modeling

(MKM) using the CHE model. At (a) pH = 13, (b) pH = 7.2 and (c) pH = 0. The relative r_{NH_3} is obtained by dividing the r_{NH_3} by its maximum. The relative r_{NH_3} and coverage are shown in upper and lower panels, respectively.

To verify the critical effects of potential-dependent binding energies, we also performed the MKM simulations using the binding energies obtained by the CHE model (Fig. 5). We find that the MKM simulations using the CHE model do not agree with the experiment. The premature decrease of r_{NH_3} and noticeable change in active site coverages are not observed. Due to the constant charge constraint in the CHE model, the slope (ΔG vs. U) for a reaction with and without proton-coupled electron transfer step is rigid at 1 and 0, respectively. Thus, fractional charge transfer that can occur during the reaction (e.g. adsorption and desorption) which does not involve proton-coupled electron transfer cannot be described in CHE model. The neutral state calculations in the CHE model would not sufficiently describe the electronic energy of ionic species such as H_3O^+ and OH^- (Supplementary Note 3 and Supplementary Fig. 5). In contrast, in the CEP model, charge is not fixed and can vary at each reaction step. The slopes

of all chemical reactions are rigorously calculated, thus the CEP model describes well the electrochemical catalytic activity in the presence of competing reactions.

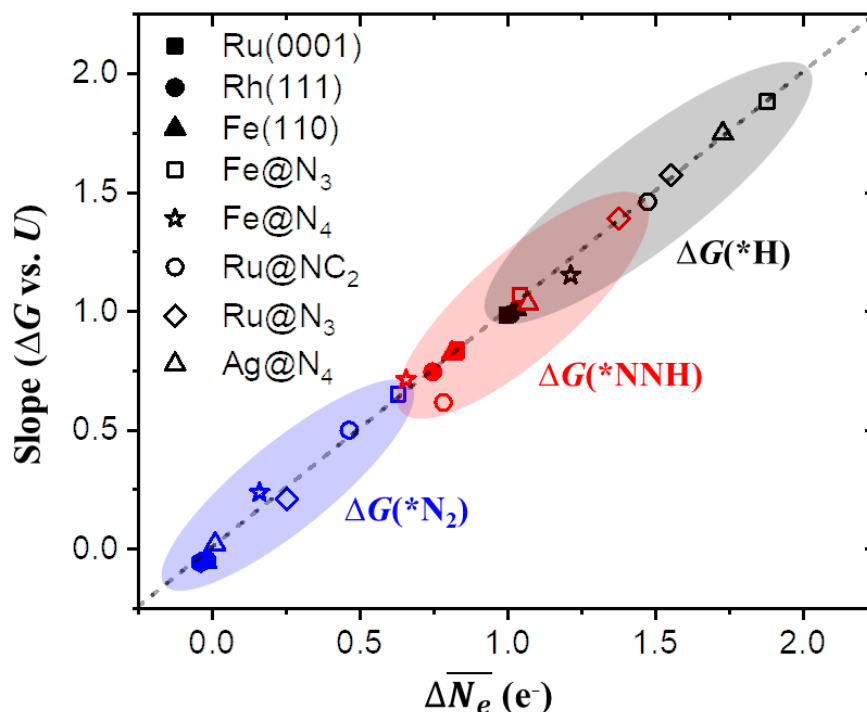


Fig. 6 | Linear correlation between the slope (the rate of change in ΔG with potential) and $\overline{\Delta N_e}$ for $\Delta G(*H)$, $\Delta G(*N_2)$ and $\Delta G(*NNH)$. Black, red, and blue colors represent $\Delta G(*H)$, $\Delta G(*N_2)$ and $\Delta G(*NNH)$, respectively. The diagonal dashed line indicates the location at slope $(\Delta G \text{ vs. } U) = \overline{\Delta N_e}$.

Origin and descriptor for different slopes. In the previous sections, we found that the change of $\Delta G(*H)$ with potential ($\Delta G \text{ vs. } U$) with a steeper slope than $\Delta G(*N_2)$ and $\Delta G(*NNH)$ leads to the surface coverage crossover and premature decrease of NRR activity. To understand the origin of these different slopes, we consider the fundamental Nernst equation. From the Nernst equation [$\Delta G \text{ (in eV)} = -\overline{\Delta N_e} U$], the first derivative of the ΔG with

respect to U is $d(\Delta G)/dU = -\Delta N_e$, where the ΔN_e represents the amount of transferred electrons in the reaction, and thus we compared the average value of ΔN_e (denoted as $\overline{\Delta N_e}$) with the computed slopes obtained for key reactions ($\Delta G(*H)$, $\Delta G(*N_2)$, $\Delta G(*NNH)$). We further consider other catalysts such as Ru(0001), Rh(111), Fe(110), Ru@N₃, Ru@NC₂, Fe@N₃ and Ag@N₄. Details on calculating slope and $\overline{\Delta N_e}$ are in Supplementary Note 6 and Supplementary Fig. 11-12). The latter catalysts are chosen since their NRR activity and their volcano-like trend were experimentally observed (Ru nanoparticles⁸, Rh nanosheet¹¹, Fe foil¹⁰ and M-NC catalysts^{15-17,23}). The computed $\overline{\Delta N_e}$ is in excellent agreement with the slope for all catalysts considered here, indicating that $\overline{\Delta N_e}$ indeed determines the potential-dependent adsorption behavior (Fig. 6). Thus, the reactions with more electron transfer become energetically more favorable as the potential becomes more negative.

Interestingly, the $\overline{\Delta N_e}$ increases in the order of $\Delta G(*N_2) < \Delta G(*NNH) < \Delta G(*H)$ for all catalysts, indicating that the key-reactions for NRR (N₂ adsorption and *NNH formation) involve fewer electrons than *H formation. These catalysts will show the coverage crossover as discussed above since the tendency of *H formation increases faster than that of *N₂ and *NNH formation with more reduction potential, resulting in the early drop of NRR activity. Thus, the coverage crossover is an intrinsic property of active site and generalizes in various catalysts.

The control of reaction selectivity between NRR and HER has been extensively studied in fields of biochemistry, bio-electrochemistry, molecular catalysis, and electrochemistry⁴⁶⁻⁴⁸. It has also been known that natural N₂-fixation catalyst, e.g. FeMo-cofactor, performs the NRR with a significant reaction selectivity up to 75%, in a subtly controlled organisms^{49,50}. In electrocatalysis, the design of entire catalytic system including catalytic active surfaces,

supporting promoters, electrolytes, and reaction conditions must also be tuned to achieve a considerable NRR selectivity and to overcome the coverage crossover between $*N_2$ and $*H$. As the fine-tuning of NRR selectivity over HER has been demonstrated in metal-complex catalysis, more delicate design of binary, tertiary, or multi-component electrocatalysts can regulate the $*H$ formation over the $*N_2$ or $*NNH$ production⁴⁷. More practically, controlling the concentration of N_2 and H^+ at the electrode-electrolyte interface with increasing the $*H$ formation barrier could be helpful, such as by the coatings with a hydrophobic layer⁵¹, utilizing polar aprotic ionic solvent (high N_2 solubility)^{52,53}, using gas diffusion electrode (high N_2 concentration)⁵⁴ or using bulky proton donor in nonaqueous electrolytes^{55,56}.

Discussion

In this study, we investigated the origin of decreasing NRR activity with potential, a major obstacle to practical NRR, generally occurring in most heterogeneous metal catalysts. The key aspect is shown to be the potential-dependent crossover in the H vs. N_2 binding affinities and associated active site coverages (initially favoring $*N_2$ but, with more negative potential, favoring $*H$). The degree of charge transfer involved in the respective reaction, consistent with the Nernst equation, is responsible for the crossover behavior in general for various catalysts. We expect the degree of charge transfer to be a simple and general descriptor to understand other electrochemical reactions and their potential dependency, such as CO_2 reduction to various products⁵⁷ and oxygen reduction reaction to H_2O vs. H_2O_2 ⁵⁸.

Methods

Computational details. All calculations were performed using spin-polarized density-functional theory (DFT) methods implemented in the Vienna Ab initio Simulation Package (VASP) with projector-augmented wave pseudopotential (PAW)⁵⁹⁻⁶¹. We used the revised PBE functional developed by Hammer *et al* (RPBE)^{62,63}. Cutoff energy was set to 400 eV. The convergence criteria for the electronic energy difference and forces are 10^{-5} eV and 0.05 eV / Å, respectively. Transition state optimization was performed using the climbing image nudged elastic band (CI-NEB)^{64,65} and improved dimer methods (IDM)^{66,67}.

Implicit solvation calculations of the electrolyte are performed using the generalized Poisson-Boltzmann model implemented in the VASPsol^{68,69}, extension of VASP. The relative permittivity of the bulk solvent chosen as that of water (78.4). We set the Debye length by 3 Å, corresponding to a 1 M concentration of electrolyte. We further added QV correction to the electronic energy, where the Q and V represent the net charge of the slab model and the negative value of the electrostatic potential at bulk electrolyte, respectively. This correction is a missing contribution to the total energy in the present VASPsol release and makes that the ΔG become independent on cell size.

The M@N_xC_y site is constructed by using a rectangular graphene supercell containing 32 carbon atoms. The transition metal surfaces are modeled by (3x3) atomic supercell with 4 layers. The bottom two layers were fixed to their optimized bulk positions, while other atoms were fully relaxed. All slab models include more than 18 Å of vacuum in the c-axis. (4x3x1) and (3x3x1) Monkhorst-Pack mesh of k-points⁷⁰ were sampled for M@N_xC_y and transition metal surfaces, respectively.

The electrode potential (U) referenced to that of standard hydrogen electrode (SHE) is given by

$$U = \frac{-\mu_e - \Phi_{\text{SHE}}}{e} \quad (1)$$

where μ_e and Φ_{SHE} represent the chemical potential of electron and work function of the SHE, respectively. We used 4.43 eV for Φ_{SHE} , obtained by the RPBE⁷¹. Also, the 4.43 eV lies within the experimentally obtained Φ_{SHE} (4.44 ± 0.02 eV)⁷². The μ_e is equal to the Fermi level compared to the electrostatic potential at bulk electrolyte. In the CEP model, the number of electrons (N_e) is adjusted to guarantee different states to have the same μ_e in the grand canonical states. Thus, we adjust N_e to match the U of the slab model with target potential (U_{target}). We set the convergence criteria for U as $|U - U_{\text{target}}| < 10^{-4}$ V.

If the two different slab model have identical μ_e , while they have different N_e , grand canonical electronic energy (Ω) is given by^{33,34}

$$\Omega = E_{\text{DFT}} - N_e \mu_e \quad (2)$$

E_{DFT} represents the electronic total energy of the slab model (in non-zero charge state). We obtained free energy (G) by using thermal energy correction to Ω .

Data availability

The main data supporting the findings of this study are contained within the paper and its associated Supporting Information. All other data are available from the corresponding author upon request.

REFERENCES

1. Mineral commodity summaries 2020. 204 (Reston, VA, 2020).
2. Saadatjou, N., Jafari, A. & Sahebdehfar, S. Ruthenium nanocatalysts for ammonia synthesis: a review. *Chem. Eng. Commun.* **202**, 420-448 (2015).
3. Philibert, C. Renewable energy for industry. *Paris: International Energy Agency* (2017).
4. Van der Ham, C. J., Koper, M. T. & Hetterscheid, D. G. Challenges in reduction of dinitrogen by proton and electron transfer. *Chem. Soc. Rev.* **43**, 5183-5191 (2014).
5. Greenlee, L. F., Renner, J. N. & Foster, S. L. The use of controls for consistent and accurate measurements of electrocatalytic ammonia synthesis from dinitrogen. *ACS Catal.* **8**, 7820-7827 (2018).
6. Montoya, J. H., Tsai, C., Vojvodic, A. & Nørskov, J. K. The challenge of electrochemical ammonia synthesis: A new perspective on the role of nitrogen scaling relations. *ChemSusChem* **8**, 2180-2186 (2015).
7. Hu, L., Xing, Z. & Feng, X. Understanding the Electrocatalytic Interface for Ambient Ammonia Synthesis. *ACS Energy Lett.* **5**, 430-436 (2020).
8. Wang, D. *et al.* Energy-Efficient Nitrogen Reduction to Ammonia at Low Overpotential in Aqueous Electrolyte under Ambient Conditions. *ChemSusChem* **11**, 3416-3422 (2018).
9. Yang, D., Chen, T. & Wang, Z. Electrochemical reduction of aqueous nitrogen (N₂) at a low overpotential on (110)-oriented Mo nanofilm. *J. Mater. Chem. A* **5**, 18967-18971 (2017).
10. Hu, L. *et al.* Ambient electrochemical ammonia synthesis with high selectivity on Fe/Fe oxide catalyst. *ACS Catal.* **8**, 9312-9319 (2018).
11. Liu, H.-M. *et al.* Surfactant-free atomically ultrathin rhodium nanosheet nanoassemblies for efficient nitrogen electroreduction. *J. Mater. Chem. A* **6**, 3211-3217 (2018).
12. Chen, Y. *et al.* Highly Productive Electrosynthesis of Ammonia by Admolecule-Targeting Single Ag Sites. *ACS Nano* **14**, 6938-6946 (2020).
13. Zhang, R., Jiao, L., Yang, W., Wan, G. & Jiang, H.-L. Single-atom catalysts templated by metal-organic frameworks for electrochemical nitrogen reduction. *J. Mater. Chem. A* **7**, 26371-26377 (2019).
14. Wang, M. *et al.* Over 56.55% Faradaic efficiency of ambient ammonia synthesis enabled by positively shifting the reaction potential. *Nat. Commun.* **10**, 1-8 (2019).
15. Tao, H. *et al.* Nitrogen fixation by Ru single-atom electrocatalytic reduction. *Chem* **5**, 204-214 (2019).

16. Wang, Y. *et al.* Rational design of Fe–N/C hybrid for enhanced nitrogen reduction electrocatalysis under ambient conditions in aqueous solution. *ACS Catal.* **9**, 336-344 (2018).
17. Geng, Z. *et al.* Achieving a Record-High Yield Rate of 120.9 $\mu\text{g}_{\text{NH}_3} \text{mg}^{-1}\text{cat. h}^{-1}$ for N_2 Electrochemical Reduction over Ru Single-Atom Catalysts. *Adv. Mater.* **30**, 1803498 (2018).
18. Sun, Z. *et al.* Oxygen vacancy enables electrochemical N_2 fixation over WO_3 with tailored structure. *Nano Energy* **62**, 869-875 (2019).
19. Han, Z. *et al.* Activated TiO_2 with tuned vacancy for efficient electrochemical nitrogen reduction. *Appl. Catal. B* **257**, 117896 (2019).
20. Zhang, M. *et al.* Reduced graphene oxides with engineered defects enable efficient electrochemical reduction of dinitrogen to ammonia in wide pH range. *Nano Energy* **68**, 104323 (2020).
21. Yu, X. *et al.* Boron-doped graphene for electrocatalytic N_2 reduction. *Joule* **2**, 1610-1622 (2018).
22. Fan, Q. *et al.* High-yield production of few-layer boron nanosheets for efficient electrocatalytic N_2 reduction. *Chem. Commun.* **55**, 4246-4249 (2019).
23. Lü, F. *et al.* Nitrogen-coordinated single Fe sites for efficient electrocatalytic N_2 fixation in neutral media. *Nano Energy* **61**, 420-427 (2019).
24. Ju, W. *et al.* Understanding activity and selectivity of metal-nitrogen-doped carbon catalysts for electrochemical reduction of CO_2 . *Nat. Commun.* **8**, 1-9 (2017).
25. Tayyebi, E., Abghoui, Y. & Skulason, E. Elucidating the mechanism of electrochemical N_2 reduction at the Ru(0001) electrode. *ACS Catal.* **9**, 11137-11145 (2019).
26. Back, S. & Jung, Y. On the mechanism of electrochemical ammonia synthesis on the Ru catalyst. *Phys. Chem. Chem. Phys.* **18**, 9161-9166 (2016).
27. Maheshwari, S., Rostamikia, G. & Janik, M. J. Elementary kinetics of nitrogen electroreduction on Fe surfaces. *J. Chem. Phys.* **150**, 041708 (2019).
28. Abghoui, Y., Garden, A. L., Howalt, J. G., Vegge, T. & Skúlason, E. Electroreduction of N_2 to ammonia at ambient conditions on mononitrides of Zr, Nb, Cr, and V: A DFT guide for experiments. *ACS Catal.* **6**, 635-646 (2016).
29. Howalt, J. G. & Vegge, T. Electrochemical ammonia production on molybdenum nitride nanoclusters. *Phys. Chem. Chem. Phys.* **15**, 20957-20965 (2013).
30. Howalt, J. G., Bligaard, T., Rossmeisl, J. & Vegge, T. DFT based study of transition metal nano-clusters for electrochemical NH_3 production. *Phys. Chem. Chem. Phys.* **15**, 7785-7795 (2013).
31. Rostamikia, G., Maheshwari, S. & Janik, M. J. Elementary kinetics of nitrogen electroreduction to ammonia on late transition metals. *Catal. Sci. Technol.* **9**, 174-181 (2019).
32. Nørskov, J. K. *et al.* Origin of the overpotential for oxygen reduction at a fuel-cell cathode. *J. Phys. Chem. B* **108**, 17886-17892 (2004).
33. Gauthier, J. A. *et al.* Challenges in modeling electrochemical reaction energetics with polarizable continuum models. *ACS Catal.* **9**, 920-931 (2018).
34. Garza, A. J., Bell, A. T. & Head-Gordon, M. Mechanism of CO_2 reduction at copper surfaces: pathways to C_2 products. *ACS Catal.* **8**, 1490-1499 (2018).

35. Xiao, H., Cheng, T. & Goddard III, W. A. Atomistic mechanisms underlying selectivities in C₁ and C₂ products from electrochemical reduction of CO on Cu(111). *J. Am. Chem. Soc.* **139**, 130-136 (2017).
36. Cheng, T., Xiao, H. & Goddard, W. A. Full atomistic reaction mechanism with kinetics for CO reduction on Cu(100) from ab initio molecular dynamics free-energy calculations at 298 K. *Proc. Natl. Acad. Sci.* **114**, 1795-1800 (2017).
37. Goodpaster, J. D., Bell, A. T. & Head-Gordon, M. Identification of possible pathways for C–C bond formation during electrochemical reduction of CO₂: new theoretical insights from an improved electrochemical model. *J. Phys. Chem. Lett.* **7**, 1471-1477 (2016).
38. Cheng, T., Xiao, H. & Goddard III, W. A. Reaction mechanisms for the electrochemical reduction of CO₂ to CO and formate on the Cu(100) surface at 298 K from quantum mechanics free energy calculations with explicit water. *J. Am. Chem. Soc.* **138**, 13802-13805 (2016).
39. Van den Bossche, M., Skúlason, E., Rose-Petruck, C. & Jónsson, H. Assessment of Constant-Potential Implicit Solvation Calculations of Electrochemical Energy Barriers for H₂ Evolution on Pt. *J. Phys. Chem. C* **123**, 4116-4124 (2019).
40. Nie, S., Feibelman, P. J., Bartelt, N. & Thürmer, K. Pentagons and heptagons in the first water layer on Pt (111). *Phys. Rev. Lett.* **105**, 026102 (2010).
41. Ren, J. & Meng, S. Atomic structure and bonding of water overlayer on Cu (110): The borderline for intact and dissociative adsorption. *J. Am. Chem. Soc.* **128**, 9282-9283 (2006).
42. Ogasawara, H. *et al.* Structure and bonding of water on Pt (111). *Phys. Rev. Lett.* **89**, 276102 (2002).
43. Vijay, S. *et al.* Dipole-field interactions determine the CO₂ reduction activity of 2D Fe-NC single atom catalysts. *ACS Catal.* **10**, 7826-7835 (2020).
44. Garcia-Ratés, M. & López, N. Multigrid-based methodology for implicit solvation models in periodic DFT. *J. Chem. Theory Comput.* **12**, 1331-1341 (2016).
45. Choi, J. *et al.* Identification and elimination of false positives in electrochemical nitrogen reduction studies. *Nat. Commun.* **11**, 1-10 (2020).
46. Barahona, E., Jiménez-Vicente, E. & Rubio, L. M. Hydrogen overproducing nitrogenases obtained by random mutagenesis and high-throughput screening. *Sci. Rep.* **6**, 1-10 (2016).
47. Benedek, Z., Papp, M., Oláh, J. & Szilvási, T. Exploring Hydrogen Evolution Accompanying Nitrogen Reduction on Biomimetic Nitrogenase Analogs: Can Fe–N_xH_y Intermediates Be Active Under Turnover Conditions? *Inorg. Chem.* **58**, 7969-7977 (2019).
48. Matson, B. D. & Peters, J. C. Fe-mediated HER vs N₂RR: Exploring factors that contribute to selectivity in P₃^EFe (N₂) (E= B, Si, C) catalyst model systems. *ACS Catal.* **8**, 1448-1455 (2018).
49. Yandulov, D. V. & Schrock, R. R. Catalytic reduction of dinitrogen to ammonia at a single molybdenum center. *Science* **301**, 76-78 (2003).
50. Hoffman, B. M., Lukoyanov, D., Yang, Z.-Y., Dean, D. R. & Seefeldt, L. C. Mechanism of nitrogen fixation by nitrogenase: the next stage. *Chem. Rev.* **114**, 4041-4062 (2014).

51. Lee, H. K. *et al.* Favoring the unfavored: Selective electrochemical nitrogen fixation using a reticular chemistry approach. *Sci. Adv.* **4**, eaar3208 (2018).
52. Suryanto, B. H. *et al.* Rational electrode–electrolyte design for efficient ammonia electrosynthesis under ambient conditions. *ACS Energy Lett.* **3**, 1219-1224 (2018).
53. Zhou, F. *et al.* Electro-synthesis of ammonia from nitrogen at ambient temperature and pressure in ionic liquids. *Energy Environ. Sci.* **10**, 2516-2520 (2017).
54. Lazouski, N., Chung, M., Williams, K., Gala, M. L. & Manthiram, K. Non-aqueous gas diffusion electrodes for rapid ammonia synthesis from nitrogen and water-splitting-derived hydrogen. *Nat. Catal.* **3**, 463-469 (2020).
55. Zhang, L. *et al.* A theoretical study of the effect of a non-aqueous proton donor on electrochemical ammonia synthesis. *Phys. Chem. Chem. Phys.* **20**, 4982-4989 (2018).
56. Singh, A. R. *et al.* Electrochemical Ammonia Synthesis-The Selectivity Challenge. *ACS Catal.* **7**, 706-709 (2017).
57. Fan, Q. *et al.* Electrochemical CO₂ reduction to C₂₊ species: heterogeneous electrocatalysts, reaction pathways, and optimization strategies. *Mater. Today Energy* **10**, 280-301 (2018).
58. Jung, E. *et al.* Atomic-level tuning of Co–N–C catalyst for high-performance electrochemical H₂O₂ production. *Nat. Mater.* **19**, 436–442 (2020).
59. Kresse, G. & Joubert, D. From ultrasoft pseudopotentials to the projector augmented-wave method. *Phys. Rev. B* **59**, 1758-1775 (1999).
60. Kresse, G. & Furthmüller, J. Efficiency of ab-initio total energy calculations for metals and semiconductors using a plane-wave basis set. *Comput. Mater. Sci.* **6**, 15-50 (1996).
61. Blöchl, P. E. Projector augmented-wave method. *Phys. Rev. B* **50**, 17953-17979 (1994).
62. Hammer, B., Hansen, L. B. & Nørskov, J. K. Improved adsorption energetics within density-functional theory using revised Perdew-Burke-Ernzerhof functionals. *Phys. Rev. B* **59**, 7413-7421 (1999).
63. Perdew, J. P., Burke, K. & Ernzerhof, M. Generalized gradient approximation made simple. *Phys. Rev. Lett.* **77**, 3865-3868 (1996).
64. Henkelman, G., Uberuaga, B. P. & Jónsson, H. A climbing image nudged elastic band method for finding saddle points and minimum energy paths. *J. Chem. Phys.* **113**, 9901-9904 (2000).
65. Henkelman, G. & Jónsson, H. Improved tangent estimate in the nudged elastic band method for finding minimum energy paths and saddle points. *J. Chem. Phys.* **113**, 9978-9985 (2000).
66. Heyden, A., Bell, A. T. & Keil, F. J. Efficient methods for finding transition states in chemical reactions: Comparison of improved dimer method and partitioned rational function optimization method. *J. Chem. Phys.* **123**, 224101 (2005).
67. Henkelman, G. & Jónsson, H. A dimer method for finding saddle points on high dimensional potential surfaces using only first derivatives. *J. Chem. Phys.* **111**, 7010-7022 (1999).
68. Mathew, K., Kolluru, V. C., Mula, S., Steinmann, S. N. & Hennig, R. G. Implicit self-consistent electrolyte model in plane-wave density-functional theory. *J. Chem. Phys.* **151**, 234101 (2019).

69. Mathew, K., Sundararaman, R., Letchworth-Weaver, K., Arias, T. & Hennig, R. G. Implicit solvation model for density-functional study of nanocrystal surfaces and reaction pathways. *J. Chem. Phys.* **140**, 084106 (2014).
70. Monkhorst, H. J. & Pack, J. D. Special points for Brillouin-zone integrations. *Phys. Rev. B* **13**, 5188 (1976).
71. Jinnouchi, R. & Anderson, A. B. Aqueous and surface redox potentials from self-consistently determined Gibbs energies. *J. Phys. Chem. C* **112**, 8747-8750 (2008).
72. Trasatti, S. The absolute electrode potential: an explanatory note (Recommendations 1986). *Pure and Applied Chemistry* **58**, 955-966 (1986).

Acknowledgements

We acknowledge generous financial support from NRF Korea (NRF-2016M3D1A1021147, NRF-2019M3D3A1A01069099).

Author contributions

C.C.[‡] and G.G.[‡] equally contributed in this work. C.C., G.G. and Y.J. conceptualized the idea and wrote the manuscript. C.C. performed DFT calculations and analyzed the result. G.G. performed MKM simulations. All authors discussed the results and assisted during manuscript preparation.

Competing interests

The authors declare no competing interest.

Additional information

Supplementary Information is available for this paper at <http://www.nature.com/ncomms>

Figures

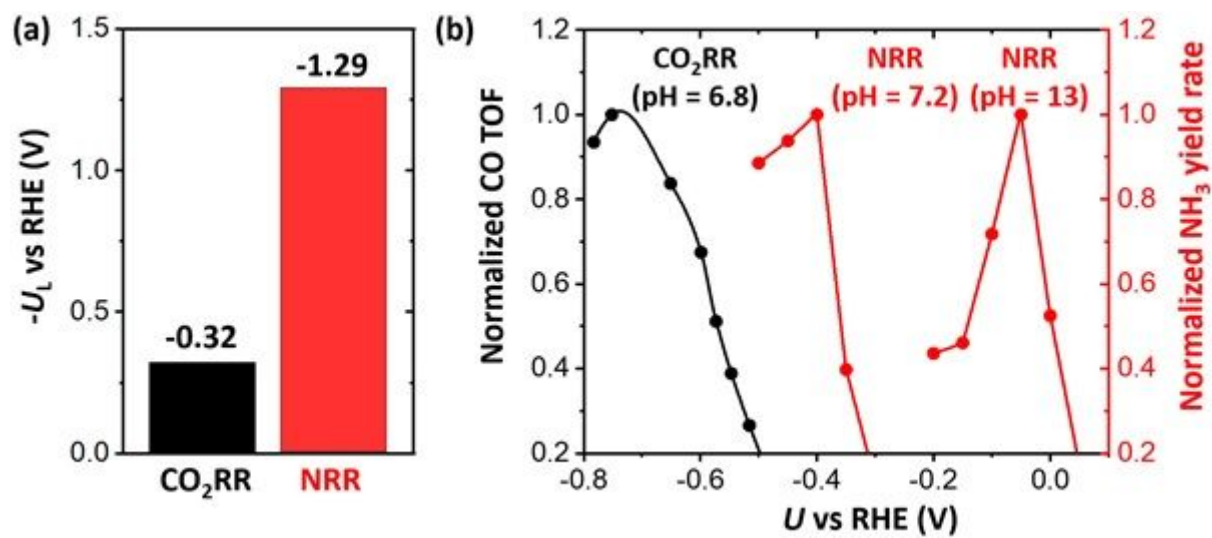


Figure 1

(see Manuscript file for figure legend)

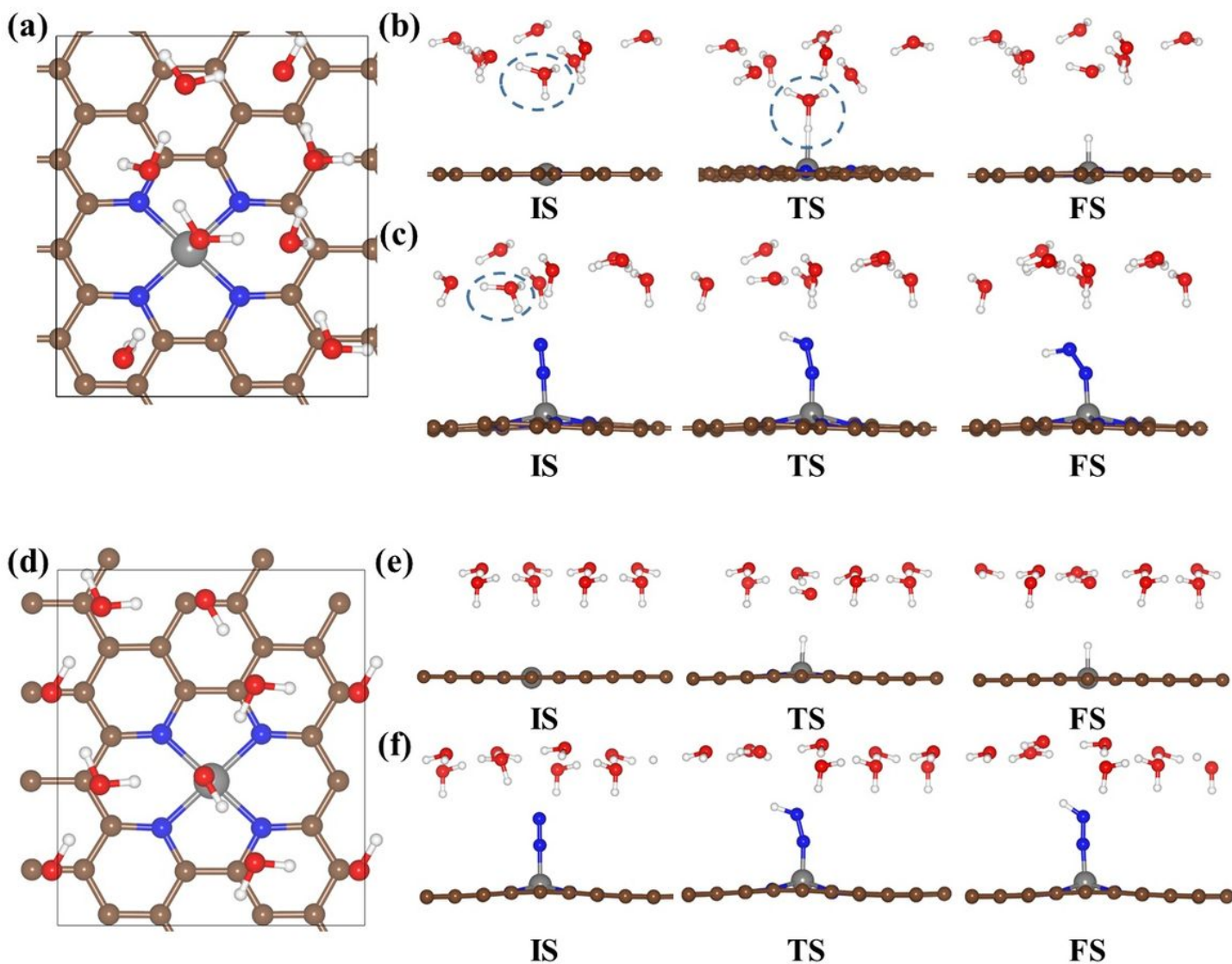


Figure 2

(see Manuscript file for figure legend)

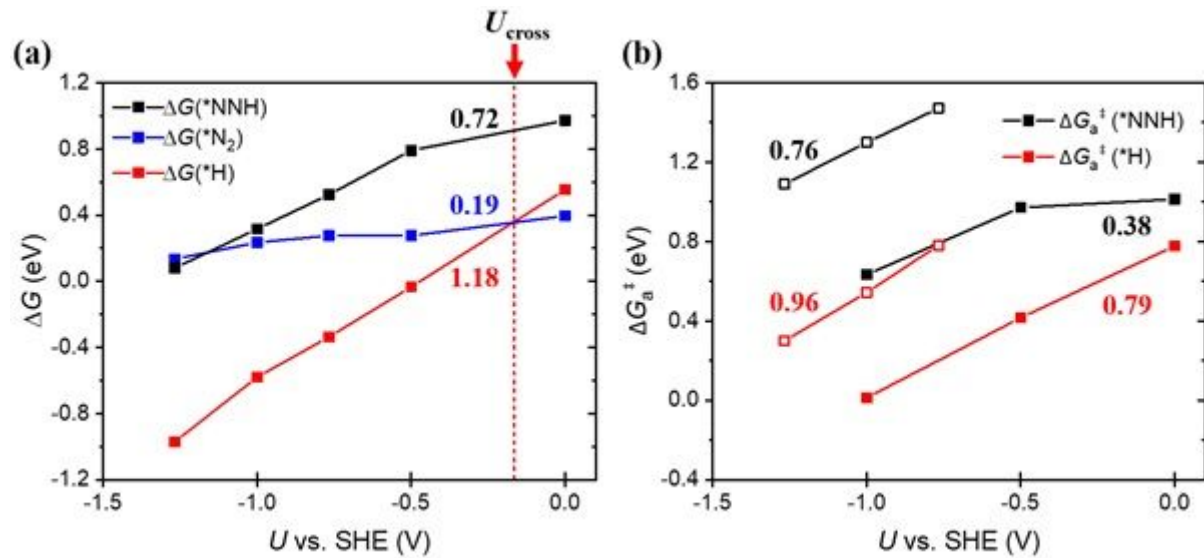


Figure 3

(see Manuscript file for figure legend)

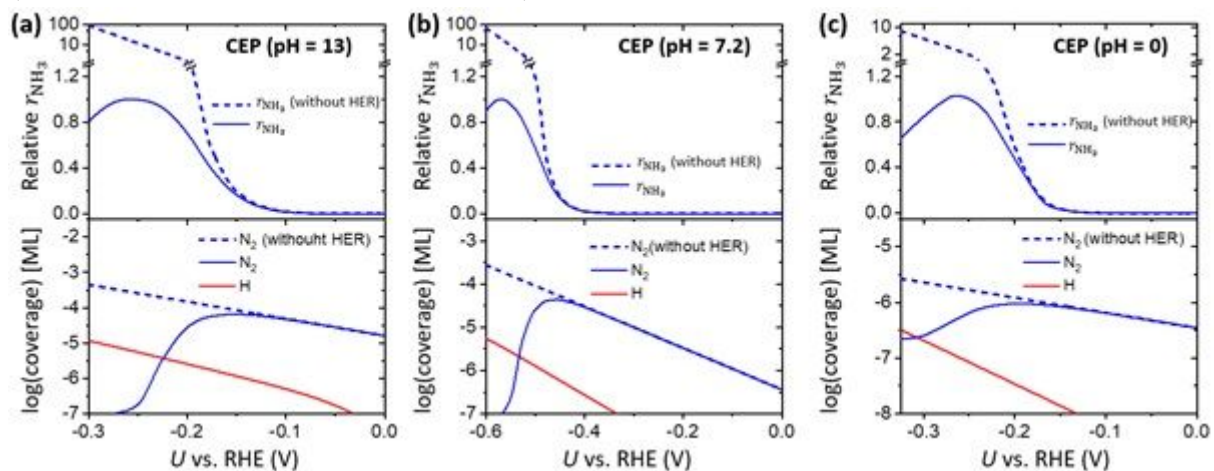


Figure 4

(see Manuscript file for figure legend)

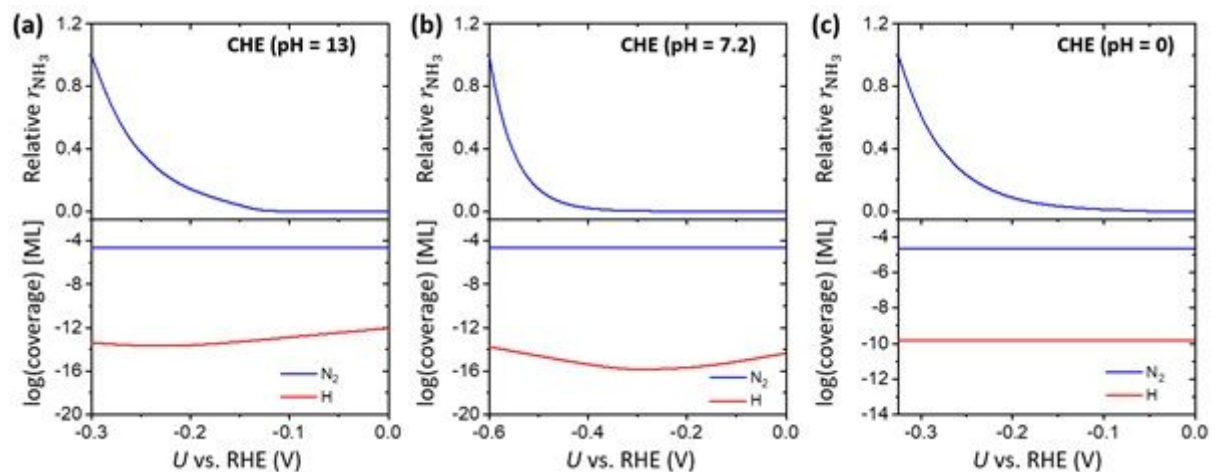


Figure 5

(see Manuscript file for figure legend)

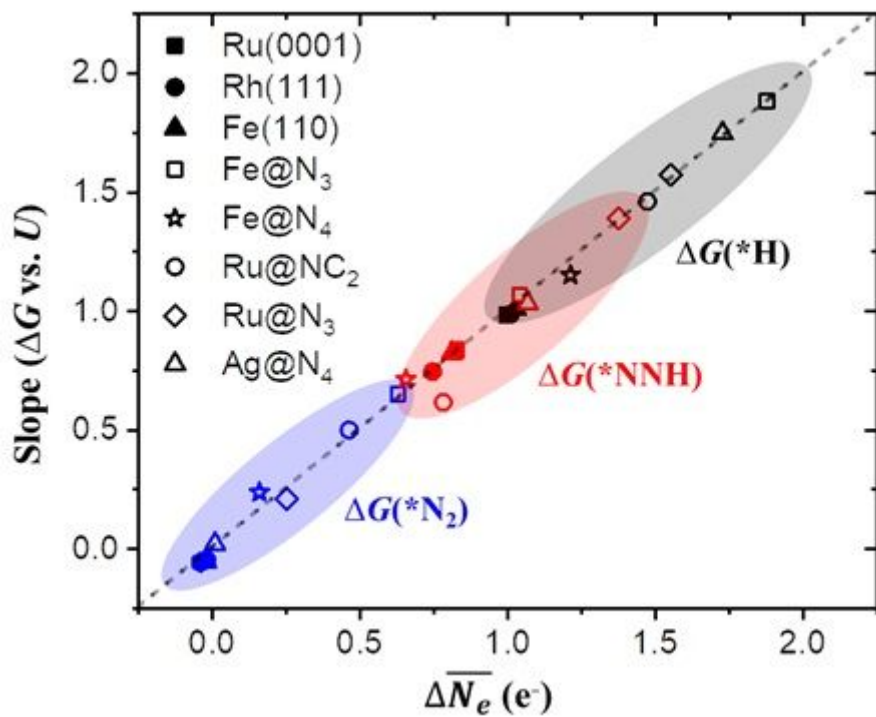


Figure 6

(see Manuscript file for figure legend)

Supplementary Files

This is a list of supplementary files associated with this preprint. Click to download.

- [S1submit.docx](#)